

Article

C-Band and X-Band Switchable Frequency-Selective Surface

Umer Farooq ¹, Adnan Iftikhar ¹, Muhammad Farhan Shafique ², Muhammad Saeed Khan ¹, Adnan Fida ¹, Muhammad Juanid Mughal ¹ and Dimitris E. Anagnostou ^{3,*}

- ¹ Department Electrical and Computer Engineering, COMSATS University Islamabad, Islamabad 45550, Pakistan; dr.umerfarooq094@gmail.com (U.F.); adnaniftikhar@comsats.edu.pk (A.I.); mskj786@hotmail.com (M.S.K.); adnan_fida@comsats.edu.pk (A.F.); junaid.mughal@comsats.edu.pk (M.J.M.)
- ² Center for Advanced Studies in Telecommunication (CAST), COMSATS University Islamabad, Islamabad 45550, Pakistan; farhan.shafique@comsats.edu.pk
- ³ Department of Electrical Engineering, Heriot-Watt University, Edinburgh EH14 4AS, UK
- * Correspondence: d.anagnostou@hw.ac.uk

Abstract: This paper presents a highly compact frequency-selective surface (FSS) that has the potential to switch between the X-band (8 GHz–12 GHz) and C-band (4 GHz–8 GHz) for RF shielding applications. The proposed FSS is composed of a square conducting loop with inward-extended arms loaded with curved extensions. The symmetric geometry allows the RF shield to perform equally for transverse electric (TE), transverse magnetic (TM), and 45° polarizations. The unit cell has a dimension of $0.176 \lambda_0$ and has excellent angular stability up to 60°. The resonance mechanism was investigated using equivalent circuit models of the shield. The design of the unit element allowed incorporation of PIN diodes between adjacent elements for switching to a lower C-band spectrum at 6.6 GHz. The biasing network is on the bottom layer of the substrate to avoid effects on the shielding performance. A PIN diode configuration for the switching operation was also proposed. In simulations, the PIN diode model was incorporated to observe the switchable operation. Two prototypes were fabricated, and the switchable operation was demonstrated by etching copper strips on one fabricated prototype between adjacent unit cells (in lieu of PIN diodes) as a proof of the design prototypes. Comparisons among the results confirmed that the design offers high angular stability and excellent performance in both bands.

Keywords: active FSS; C-band; frequency-selective surface (FSS); spatial filters; switchable; X-band



Citation: Farooq, U.; Iftikhar, A.; Shafique, M.F.; Khan, M.S.; Fida, A.; Mughal, M.J.; Anagnostou, D.E. C-Band and X-Band Switchable Frequency-Selective Surface. *Electronics* **2021**, *10*, 476. <https://doi.org/10.3390/electronics10040476>

Academic Editor: Bang Chul Jung

Received: 1 January 2021

Accepted: 13 February 2021

Published: 17 February 2021

Publisher's Note: MDPI stays neutral with regard to jurisdictional claims in published maps and institutional affiliations.



Copyright: © 2021 by the authors. Licensee MDPI, Basel, Switzerland. This article is an open access article distributed under the terms and conditions of the Creative Commons Attribution (CC BY) license (<https://creativecommons.org/licenses/by/4.0/>).

1. Introduction

Nowadays, urban environments are saturated with electromagnetic energy produced by the wireless devices used in our daily routines. This energy is meant for limited numbers of people, but everyone is exposed to it. Apart from causing interferences for nearby devices, it may also has adverse long-term effects on human health, causing tissue damage as well as the development of tumors in the worst cases [1–5]. In secured installations, such as intensive care units (ICUs), security and military installations, operation theaters, and cardiac care units (CCUs), communication can be restricted to frequency spectra below the C-band (4 GHz–8 GHz), in which only 3G and 4G mobile connectivity is maintained. This limitation very much suffices for basic communication needs. In these systems, all higher-frequency signals, such as those in the upper 802.11ac WLAN band, as well as in some ISM bands, are desired to be rejected.

In addition, the X-band (8–12 GHz) (used in space communications and radars) is another high-frequency and high-power electromagnetic (EM) spectrum that is present in the environment and can endanger human beings. The mitigation of RF radiation in restricted zones where security is a prime concern is often required by security agencies. Therefore, to mitigate unwanted EM radiation and electromagnetic interference (EMI) in controlled environments, several methods have been practiced, such as shielding an

environment/device using metal foils or metallic coating [6]. These conventional shielding methods block useful signals along with unwanted signals, and also add additional cost, weight, and bulkiness to devices [6,7].

On the contrary, frequency-selective surfaces (FSSs) [8], due to their single- and multi-band frequency suppression characteristics, have been extensively used in military installations, secure locations such as jails, and various other sites [9,10]. In the literature, several configurations of FSSs have been reported to mitigate EMI for GSM, WLAN/Wi-Fi, and X-band signals in a single- or multi-mode operation [11–13]. In addition, frequency-reconfigurable and tunable FSSs that are capable of shielding more than two frequency bands have also been reported [14–18]. Various methods, such as mechanical deformation, material tuning, circuit biasing, and micro-fluidic techniques, have been employed to alter the frequency response of FSSs [19]. However, mechanical deformations are difficult to implement due to complexities related to their physical controls. Similarly, material tuning causes surfaces to suffer from environmental conditions, such as humidity and changes in temperature. Circuit biasing is a frequently employed method for achieving reconfiguration. Varactor and PIN diodes have been used [7,11,12]. The active shields realized using the above-mentioned techniques are extremely useful in extracting the optimal frequency spectra as per the requirements of end users. Nonetheless, the major limitations associated with these active FSSs are their polarization dependence and poor shielding performance at different angles of incidence [14–16].

The authors of [16] proposed a Jerusalem-cross-based tunable FSS with a unit cell size of 27.5 mm to shield 900 and 1800 MHz, whereas varactors were used to tune lower bands. However, the authors did not report the FSS's behavior for transverse electric (TE), transverse magnetic (TM) polarizations, or the shielding stability at normal and oblique incidence angles. In addition, a tunable meta-material FSS with 10.5 mm size was tuned from 3 to 3.5 GHz band by using varactors on both sides of the substrates [17], but polarization independence of the FSS was not established to demonstrate its suitable candidacy for practical applications. An FSS geometry with a unit cell size of 10.5 mm operating at 5.8 GHz was made reconfigurable by using a mechanical setup that altered the gaps between the FSS elements in order to attain frequency-reconfigurable operation [18]. Nevertheless, the performance of the FSS proposed in [18] at oblique incidence angles was not reported. In addition, reconfigurable FSSs using two techniques—one was based on using diodes to change the current distribution, and the second was based on mechanical rotation of the FSS—were proposed in [20]. The realizations of both techniques were performed only in simulations, which, therefore, may raise performance concerns in the practical realization of the proposed FSS shields. In [21], a venetian-blind-based shutter mechanism was used to achieve reconfigurability in an FSS, but the shutter mechanism was employed manually. Similarly, a reconfigurable dual-band-stop FSS using a liquid crystal polymer was proposed in [22] without in-depth analysis or discussions on the practical realization or angular stability. In the existing literature, only one flexible and reconfigurable FSS with angular stability has been proposed so far, which can be found in [23]. The FSS proposed in [23] was designed on flexible plastic and fabricated using an additive manufacturing process, whereas varactor diodes with a bias line on the same layer of the FSS were used to achieve frequency reconfigurability. The reported FSS offered better shielding performance by virtue of the costly additive manufacturing process, and it required extra effort to place the FSS on the host dielectric, which caused additional design bulkiness. In addition, the effect of strong coupling between RF and DC currents because of the placement of the FSS and DC bias lines on the same layers resulted in a poor shielding performance by the FSS.

It can be seen in the above literature review and discussion that, presently, FSS geometries with reconfigurability have sizes of about $2.7\lambda_0$ or more for X-band shielding [12], which is mainly because the multi-band, tunable, and reconfigurable shielding operations increase the size of the structure, and it is very hard to sustain the polarization independence and angular stability, as reported in the literature [14–18]. In this very context, the

objective of this work is to propose a highly compact and efficient FSS shield for X-band applications with an option of switching to C-band suppression. The novelty is justified because such compact FSS designs for switchable X- and C-band shielding are not available in the literature. In this paper, it is successfully demonstrated that the proposed FSS design has a stable frequency response for both the TE/TM and 45° polarizations at normal and oblique angles of incidence of up to 60°. The remainder of the paper is organized as follows: The FSS unit cell modeling and simulation results are presented in Section 2. Mathematical and equivalent circuit models of the design are presented in Section 3, whereas a parametric analysis of the design is discussed in Section 4. The proposed mechanism of active switching to the C-band is discussed in Section 5. A comparison of the simulated and measured results for various incident angles is shown in Section 6, followed by the conclusion in the last section.

2. Proposed Passive FSS Unit Cell

A schematic view of the proposed square-loop FSS with inward-extended quarter-circular arms and with optimized dimensions is shown in Figure 1a. The proposed design was realized on a single layer of a low-cost FR4 laminate with a thickness $h = 1.6$ mm, relative permittivity $\epsilon_r = 4.4$, and loss tangent $\tan\delta = 0.02$. An FSS unit cell was first modeled and optimized in a 3D full-wave EM simulator (Ansys HFSS) [24]. Initially, a conventional square loop was simulated, and its frequency response was observed. Afterwards, to miniaturize the proposed design and increase the angular stability of the proposed FSS, inward-extended quarter-circular arms were incorporated to achieve the maximum shielding effectiveness (SE) in the desired band. Furthermore, an inward-extended and curved arm was introduced to tune the shielding frequency by keeping the overall unit cell size at $4.8 \text{ mm} \times 4.8 \text{ mm}$. For the idealization of the FSS unit cell as an EM shield with infinite periodicity in the x - and y -axes, a Floquet port analysis [25] with master and slave boundaries (linked boundaries) was performed to achieve the desired shielding effectiveness for the X-band. An illustration of the Floquet analysis along with the port declaration and periodic boundary setup is presented in Figure 1b–d. Fundamentally, the Floquet modes impinge on an EM plane wave normal to the FSS, i.e., the propagation direction is set by the frequency, phasing, and geometry of the periodic structure. The simulator solution included a model decomposition with information on the performance of the radiating structure. The impinging EM waves in the Floquet modes then interrelated with the S-matrix, and the S-parameter results were computed for an infinite array under periodic boundary conditions (shown in Figure 1b–d). Next, the dB value of $|S_{21}|$ was plotted against the frequency to observe the SE of the designed FSS. The SE is often defined as the ratio of forward power transmitted by the source (P_f) to power received at the termination (P_r). Mathematically,

$$SE_{dB} = 10 \log_{10} \frac{P_f}{P_r}, \quad (1)$$

which can be further simplified and interpreted in terms of $|S_{21}|$ as:

$$SE_{dB} = -20 \log_{10} |S_{21}|. \quad (2)$$

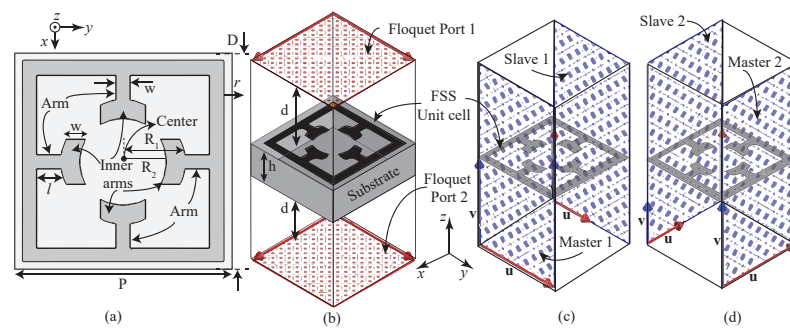


Figure 1. Unit cell geometry of the frequency-selective surface (FSS) and simulation setup for the unit cell investigation. (a) Geometry of the proposed miniaturized and symmetric FSS unit cell with optimized dimensions: $P = 4.8$ mm, $L = 4.2$ mm, $w = 0.3$ mm, $R_1 = 0.8$ mm, and $R_2 = 0.8$ mm; (b–d) FSS unit cell model with periodic boundary conditions and Floquet port assignments.

3. Equivalent Circuit Model (ECM)

To accurately predict the resonance behavior and SE of the proposed FSS, an equivalent circuit model (ECM) was extracted using the lumped element model theory [26–31], and the values were determined using the coupled-line theory [26,27]. A plane wave from port 1 (shown in Figure 1b) propagates through free space and illuminates the shield. This illumination results in surface currents at the resonant frequency around the closed loop of the FSS [27]. The free-space impedance is modeled as Z_0 (377Ω), whereas the square-loop conducting structure in the proposed FSS unit cell is modeled using inductances. For the symmetrical modeling, inductance is divided into half on both sides of the inner arms, which divide each leg of the square loop into two parts, as shown in Figure 2a. The conductive nature of the inward-extended arms is also modeled as an inductor L_{arm} , whereas the coupling capacitance C_c is incorporated to attribute the coupling between the inner extended arms. The construction and mapping of each conducting strip of the proposed FSS on the equivalent lumped elements are depicted in Figure 2a. In addition, C_{fss} in the lumped model is included to represent the coupling between the adjacent cells in a periodic structure of the proposed FSS. Since the distance between the inner extended arms is greater than the distance between the adjacent cells, the combined coupling capacitance C_c can be neglected during the subsequent circuit simplification (Figure 2c). An illustration of the lumped element model extracted from Figure 2a is depicted in Figure 2b. The impedance of the dielectric used in the unit cell is modeled by Z_T ; however, it may be neglected because of the incomparable thickness of the substrate [27].

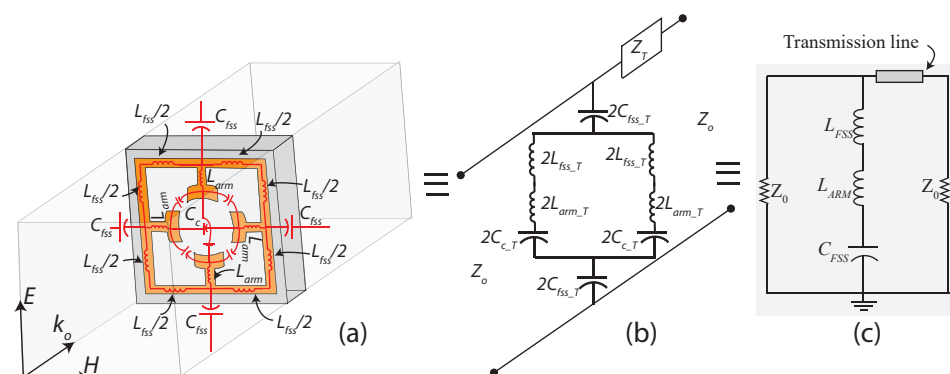


Figure 2. (a) Mapping and construction of the equivalent lumped element model of the proposed FSS unit cell, (b) the equivalent circuit model (ECM), and (c) the simplified ECM of the proposed FSS unit cell.

It can be seen in Figure 2c that the total impedance of the proposed FSS (Z_{FSS}) is a series and parallel combination of the inductances and capacitances shown in Figure 2b. Therefore, after simplification, the final construction of the ECM of the proposed FSS

is effectively a series LC circuit in parallel with the free-space impedance at both ends. Mathematically, the FSS impedance Z_{FSS} is expressed as [26,27]:

$$Z_{FSS} = X_{L_{FSS}} + X_{L_{ARM}} + X_{C_{FSS}}, \quad (3)$$

where $X_{L_{FSS}}$ is the reactance corresponding to the complete length of the square loop. $X_{C_{FSS}}$ represents the coupling between the two adjacent unit cells, and $X_{L_{ARM}}$ represents the lengths of the inner extended arms, as shown in Figure 2c. By replacing the equations for the reactances in Equation (3), we get:

$$Z_{FSS} = j\omega L_{FSS} + j\omega L_{ARM} + \frac{1}{j\omega C_{FSS}}. \quad (4)$$

Rearranging Equation (4), we obtain

$$Z_{FSS} = \frac{j^2\omega^2 L_{FSS} C_{FSS} + j^2\omega^2 L_{ARM} C_{FSS} + 1}{j\omega C_{FSS}}. \quad (5)$$

Further simplification of Equation (5) results in Equation (6):

$$Z_{FSS} = \frac{1 - (\omega^2 C_{FSS})[L_{FSS} + L_{ARM}]}{j\omega C_{FSS}}. \quad (6)$$

The shielding frequency f_r of the ECM in Equation (6) is obtained by equating the numerator to zero [29]. This implies that

$$f_r = \left(\frac{1}{2\pi}\right) \left(\sqrt{\frac{1}{C_{FSS}(L_{FSS} + L_{ARM})}}\right). \quad (7)$$

It can be interpreted from Equations (6) and (7) that the combined capacitive and inductive reactances corresponding to the distance between adjacent unit cells and conductive strips of the FSS, respectively, cancel each other at the shielding frequency f_r . The cancellation of the inductive and capacitive reactances results in a short circuit in the ECM and, consequently, reflects all EM energy that strikes the surface of the shield. In addition, for $f < f_r$, the capacitive nature of the lumped LC circuit dominates the resonance mechanism. Conversely, when the impedance of the series LC circuit is inductive at $f > f_r$, a higher shielding frequency f_r with dominant inductive impedance—as compared to the capacitive impedance of the lumped LC circuit—results. Equation (7) also shows that various combinations can be formulated using different values of inductances and capacitances through the lumped circuit theory [27]. Therefore, for the shielding frequency of 11 GHz, when optimized through 3D EM simulations, the values of the equivalent lumped elements are finalized at $C_{FSS} = 0.065$ pF, $L_{FSS} = 2.4$ nH, and $L_{ARM} = 0.8$ nH. For the verification of the ECM, values of the reactances obtained from Equation (7) were used to simulate Figure 2c in a circuit simulator [32]. A comparison between the SE of the unit cell modeled in the 3D EM software (Figure 1) and the ECM is presented in Figure 3. It shows that the EM simulation results are in good agreement with the circuit simulation results.

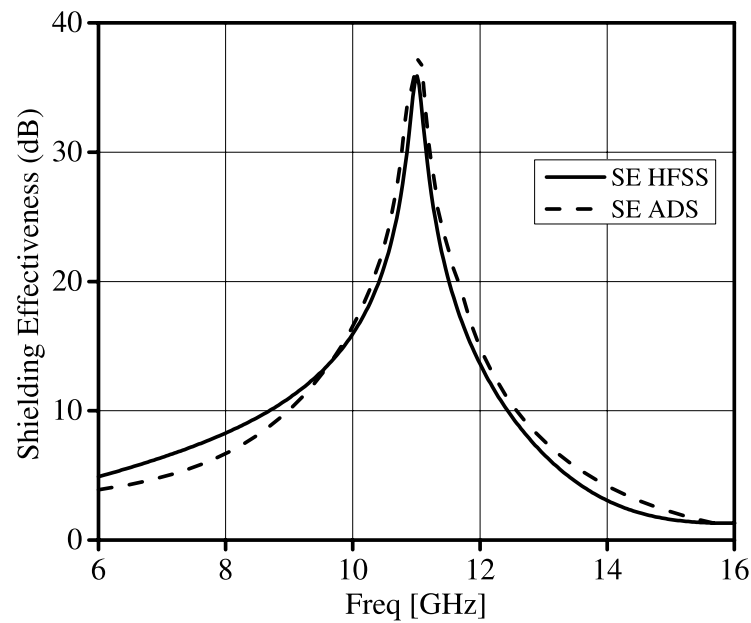


Figure 3. A comparison of the shielding effectiveness (SE) results of the EM simulation and circuit simulation.

4. Parametric Analysis

After the simulation and circuit modeling of the unit cell, a detailed parametric analysis was performed to observe the behavior of the proposed FSS with variations in the geometric parameters and dielectric constant of the substrate. Specifically, variations in the shielding frequency were investigated by varying (1) unit element size, (2) the extended arm length l , (3) the trace width w of the unit element (shown in Figure 1a), and (4) the dielectric constant ϵ_r of the substrate. It was observed that changing the FSS parameters altered the overall inductance L_{FSS} and capacitance C_{FSS} of the FSS structure. Mathematically, inductance is expressed as [31]:

$$L_{FSS} = \mu_0 \left(\frac{1}{2\pi} \right) \log_{10} \left(\frac{1}{\sin \frac{\pi w}{2D}} \right), \quad (8)$$

where μ_0 is the permeability of free space, l is the length of inner extended arms of the FSS unit cell, D is the overall length of the square loop, and w is the width of the FSS conductor. Equation (8) shows that inductance L_{FSS} has direct dependence on D , whereas an increase in width w decreases the inductance of the FSS structure. The direct and indirect dependence of the length and width of the FSS was verified by performing a parametric analysis on the length and width of the FSS unit cell in the EM simulator. Figure 4a shows the effect on shielding frequency with respect to the change in FSS length. It can be seen in Figure 4a that changing the arm length while keeping other parameters constant shifts the shielding frequency of the proposed FSS. Similarly, performing a parametric analysis on the width w of the FSS unit cell showed that inductance decreases as w increases; thus, shielding frequency shifts to the higher side, as shown in Figure 4b. Furthermore, the effect on the shielding frequency f_r was observed by changing inter-element spacing r . It was observed that an increase in r decreases the capacitance of the FSS units and results in a higher shielding frequency, as is evident in Figure 4c and the relation given in Equation (9).

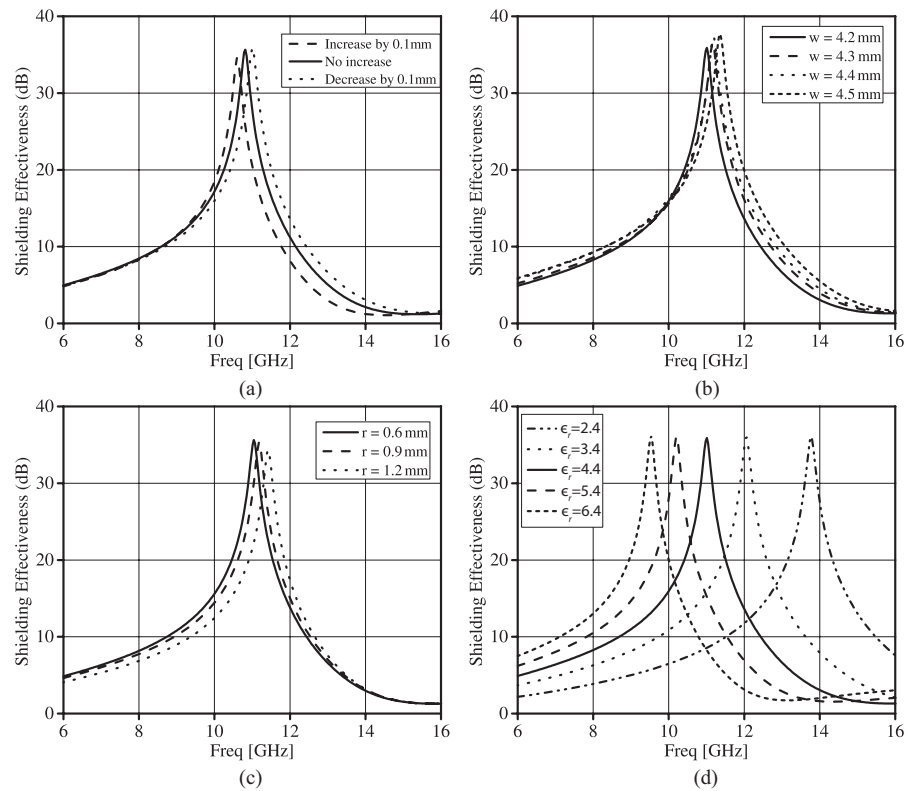


Figure 4. Parametric analysis of geometric parameters and their effects on f_r by changing the (a) arms’ length l , (b) strip width w , (c) element spacing r , and (d) dielectric constant ϵ_r .

$$C_{FSS} = \epsilon_0 \epsilon_{eff} \left(\frac{2D}{\pi} \right) \log_{10} \left(\frac{1}{\sin \frac{\pi r}{2D}} \right). \tag{9}$$

The dielectric constant ϵ_r was also varied to analyze the FSS’s performance, and the corresponding results are shown in Figure 4d. It was observed that, as the value of ϵ_r starts increasing, the f_r tends to decrease. This is because the square-loop length D is inversely related to ϵ_{eff} ; mathematically, it is represented as [12]:

$$D \approx \frac{c}{4f_r \sqrt{\epsilon_{eff}}}, \tag{10}$$

where ϵ_{eff} is the effective permittivity and is approximated as $\epsilon_{eff} = \frac{(\epsilon_r + 1)}{2}$.

Angular Stability of the FSS at Normal and Oblique Angles of Incidence

The shielding performance of the proposed FSS under a normal angle of incidence for TE and TM polarizations is presented in Figure 5. Overall, identical and stable shielding responses at the X-band were observed for both the TE and TM polarizations because of the symmetrical structure of the FSS.

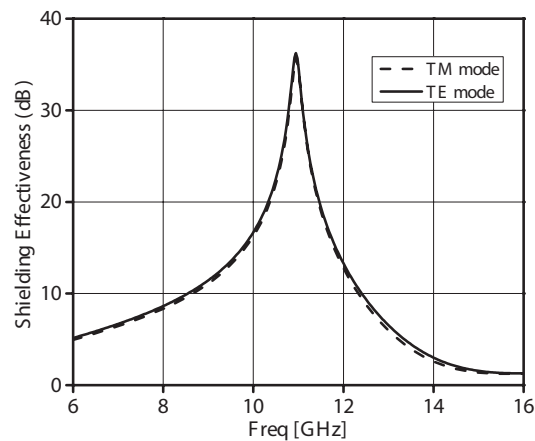


Figure 5. SE of the FSS for the transverse magnetic (TM) and transverse electric (TE) polarizations at a normal angle of incidence.

Moreover, the performance of the FSS at various angles of incidence for both the TE and TM polarizations was also analyzed to demonstrate the practicability of the FSS. For performance analysis at various angles, two Floquet ports with TE and TM modes at oblique angles (0° , 30° , and 60°) were used in the simulation model of the FSS. The results showed that the proposed FSS had a stable frequency response for TM polarization at angles varying from 0° to 60° , which correspond to higher modes. In the conventional square-loop FSS unit cell, the absence of the conductive patterns in the inner area resulted in poor angular stability. However, in the proposed FSS unit cell, four inner conductive arms with curved strips covered the inner area and provided greater angular stability for the EM waves arriving from the different angles. Thus, the extended inner arms of the proposed square-loop FSS not only tuned the shielding frequency (f_r), but also provided stability to the FSS at various angles of incidence. From Figure 6a, it can be seen that the SE increased from 35 to 39 dB as the angle of incidence was increased from 0° to 60° for TM polarization, with less than 1% change in f_r . However, for the TE polarization, slight shifts of 1.2% and 1% in f_r were observed as the angle of incidence was increased from 0° to 60° , respectively. In addition, for the TE polarization, f_r showed a stable response, as depicted in Figure 6b.

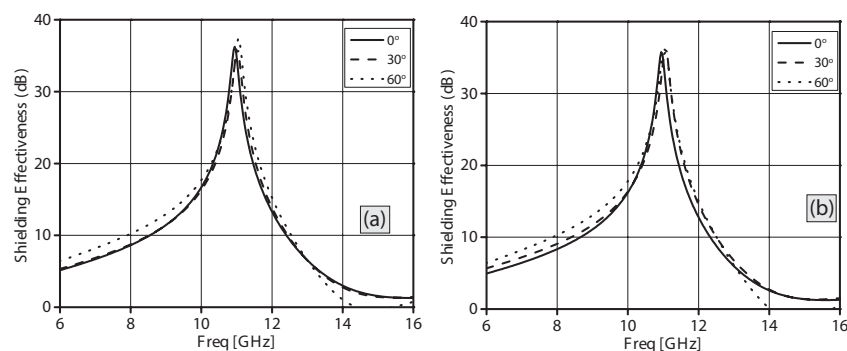


Figure 6. Shielding response of the proposed FSS at oblique angles (0° , 30° , and 60°): (a) TM polarization and (b) TE polarization.

In addition, a stable frequency response of the proposed FSS at oblique angles and changes in bandwidth at oblique angles for the TM and TE polarizations were observed because of the variation in the surface impedance at oblique angles. A 15 dB bandwidth comparison of both polarizations is shown in Table 1. It was found that bandwidth increases with an increase in the angle of incidence.

Table 1. Bandwidth comparison.

Incidence Angle	TM Polarization	TE Polarization
0°	1.90 GHz	2.05 GHz
15°	1.94 GHz	2.16 GHz
30°	2.11 GHz	2.18 GHz
45°	2.35 GHz	2.68 GHz
60°	3.27 GHz	3.25 GHz

5. Proposed Active FSS

The proposed FSS unit cell shown in Figure 1 can be reconfigured using PIN diodes (SMP-1322-079LF [33]) to suppress the C-band (6.6 GHz) instead of the X-band. Reconfigurability was achieved by incorporating PIN diodes in the gaps between the adjacent unit cells of the FSS. To demonstrate this reconfigurability, a finite 3×3 element FSS was simulated, as shown in Figure 7a. The PIN diodes were modeled as equivalent RLC boundaries between adjacent cells. The “OFF” and “ON” states of the PIN diodes in the ECM are also shown in Figure 7a. The PIN diodes act as an open circuit in the “OFF” state. However, for the “ON” state, an additional inductance appears between the unit cells, resulting in the reduction of the shielding resonant frequency to the C-band. The value of C_{fss} (Figure 2a) also changes, since there is a capacitance between the adjacent elements, but due to the imperfect nature of metallic strips, a low value of capacitance C_{fss} still exists, which results in the reduction of the resonant frequency. The response of the reconfigurable FSS is shown in Figure 7b. It can be confirmed from the figure that the FSS operates in either the X-band or C-band with the PIN diodes in the “OFF” state or “ON” state, respectively. The shielding resonant frequency for the C-band is centered at 6.6 GHz with a 15 dB bandwidth of 2.75 GHz.

Furthermore, to elaborate on the reconfigurability operation of the proposed FSS, induced surface current distributions for a 3×3 element shield are plotted in Figure 8 for both bands. The colors of the arrows show the intensity of the surface currents, while current flow is represented by the direction of arrows. It can be observed in Figure 8a that the “OFF” state of PIN diodes isolated the flow of current between adjacent elements and resulted in shielding of the X-band. However, for the “ON” state of diodes, the current flowed through them and increased the effective length, resulting in suppression of the C-band. For the TE mode, which is shown in Figure 8b, the PIN diodes in the “ON” state carried a strong current on the left and right sides, whereas a low current intensity can be observed on the top and bottom diodes of the unit element. The PIN diodes were modeled as equivalent lumped elements and simulated using RLC boundary conditions. However, in practical realization, a biasing circuitry is necessary in order to operate these PIN diodes. In this regard, a biasing mechanism was proposed to operate these diodes under forward or reverse bias conditions. The biasing network was designed on the back side of the shield with thin conductive lines, as shown in Figure 9. These conductive lines were connected to the diodes on the top layer with conductive vias; two diodes were connected to one conductive line, and the other two were connected to the other conductive line in each unit element. These pairs were isolated using capacitors to avoid short circuiting. Since the biasing circuit was on the bottom side of the FSS, the effect of the DC current on the RF current, which was on top layer, would be at its minimum, and the shielding effectiveness of the FSS would remain the same as that in the simulation results. In addition, the capacitors incorporated on each arm of the FSS in the top layer in the proposed biasing circuitry would avoid short circuiting because of any DC current leakage and would pass the RF current. However, a negligible effect on shielding effectiveness may exist because of the stray capacitance. Therefore, it can be argued that the incorporated capacitors will have a negligible effect on the overall shielding effectiveness of the proposed FSS.

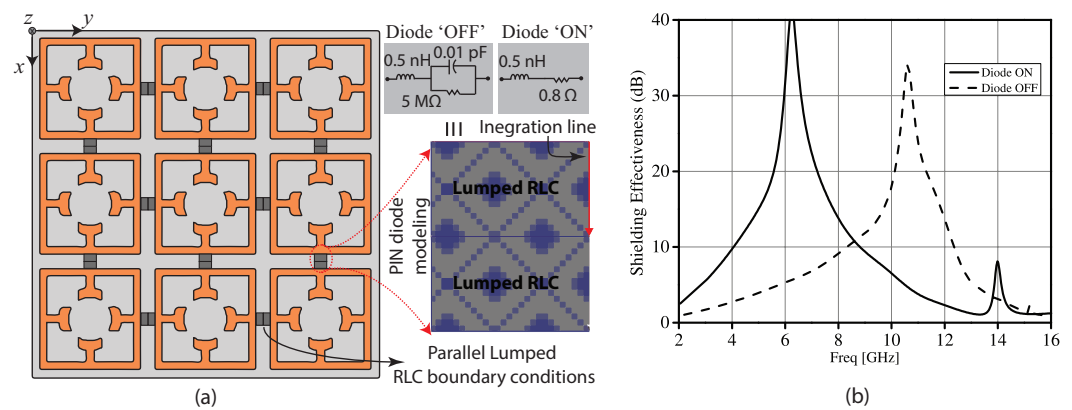


Figure 7. (a) Illustration of the reconfigurable variant of the proposed FSS and (b) the simulated SE of the proposed FSS unit cell with PIN diodes in the “OFF” and “ON” states.

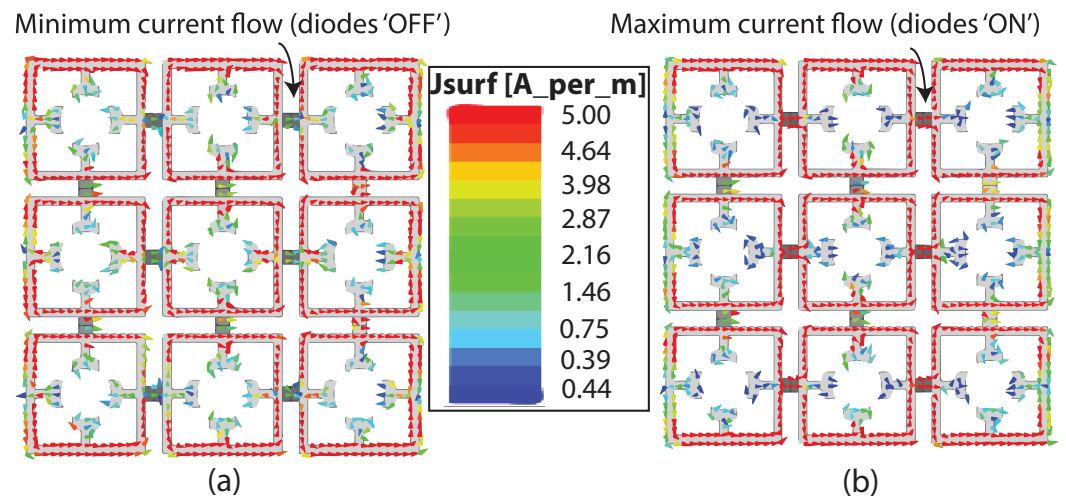


Figure 8. Surface current distribution of the reconfigurable FSS in the TE mode with (a) a PIN diode in the “OFF” state at 11 GHz and (b) a PIN diode in the “ON” state at 6.6 GHz.

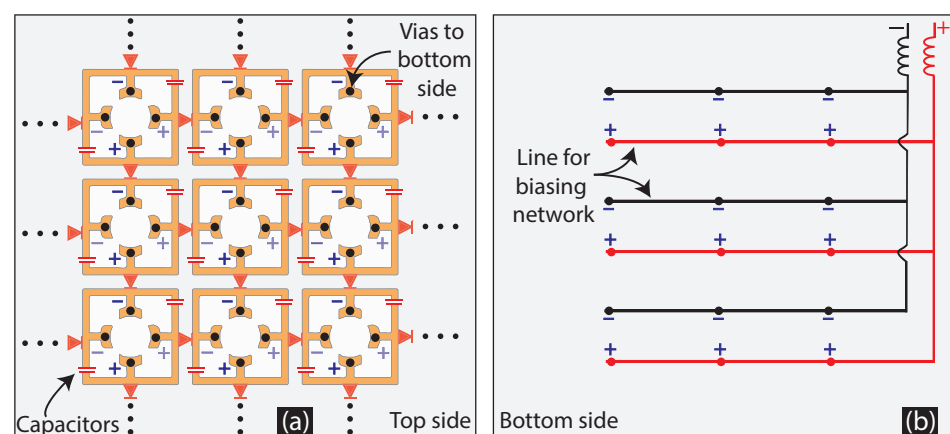


Figure 9. Biasing network topology for PIN diode switching; (a) PIN diodes’ locations and vias for connections and (b) the biasing network on the back side with RF chokes.

6. Measured Results

To validate the proposed designs, two separate shields were fabricated. One shield had no connections between unit elements, representing the “OFF” state of the PIN diodes, and the other one had shorting strips, representing the “ON” state. Both shields were

fabricated on an FR4 substrate with $\epsilon_r = 4.4$, $\tan\delta = 0.02$, and 1.6 mm thickness. Each shield had 54×52 elements. Pictures of the FSS prototypes fabricated with and without metallic strips to mimic PIN diodes' "ON" and "OFF" states, respectively, are shown in Figure 10a,b. The overall size of the fabricated prototype was $9.78\lambda_0 \times 9.32\lambda_0$ at a frequency of 11 GHz. To measure the shielding effectiveness of the fabricated prototype, a rectangular aperture with dimensions $240 \text{ mm} \times 240 \text{ mm}$ was created in an aluminum sheet with size $260 \text{ mm} \times 250 \text{ mm}$ (greater than $6\lambda_0$). This was done to ensure that the EM plane wave was only transmitted through the FSS fixed in the aperture. Two identical broadband horn antennas (model#LB-20265) [34] were used as a transmitter and receiver. A block diagram of the experimental setup used for the measurements is shown in Figure 10c. Furthermore, to ensure the efficacy and accuracy, a two-stage measurement process was adopted where, in the first stage, the reference measurement of $|S_{21}|$ was carried out through the aperture without a shield. This reference measurement was performed to measure the free-space transmission through the aperture. Then, in the second stage, the shields were placed in the aperture and measured with reference to the calibration. Similarly, for angular stability measurements, the setup was rotated at different angles.

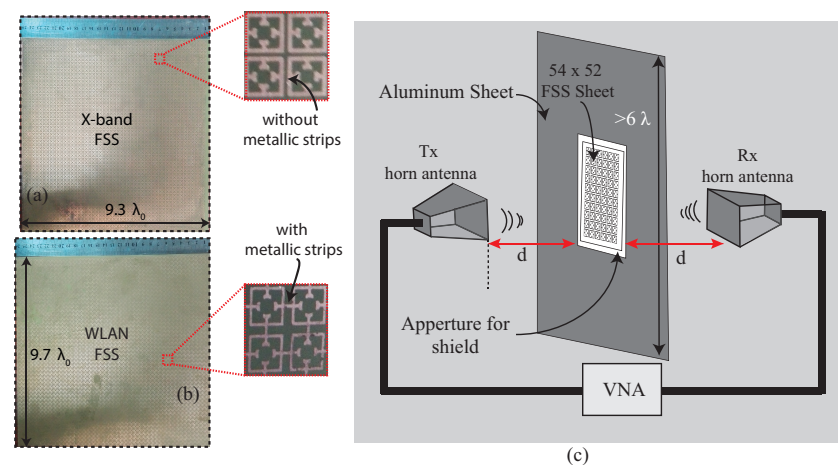


Figure 10. FSSs fabricated with 54×52 unit cells on a $260 \text{ mm} \times 250 \text{ mm}$ FR4 board: (a) FSS without metallic strips for the X-band shielding and (b) FSS with metallic strips for C-band shielding. (c) Illustration of the experimental setup for all measurements.

Performance at Normal and Oblique Angles of Incidence

A comparison of the simulated and measured results at angles of incidence of 0° , 30° , and 60° for the TE polarization is shown in Figure 11A. The results for the TM polarization at different incident angles should be the same as those in Figure 11 because of the symmetry in the design geometry. It can be seen in Figure 11A that the finite FSS sheet without metallic strips (in PIN diodes' "OFF" state) had a stable angular response for the TE/TM polarizations at the X-band. The comparison showed that the measured results are in good agreement with those of the simulations. The fabricated FSS offered 30 dB SE for the X-band. The angular stability for the 45° polarization was also measured and compared with the simulated results, as shown in Figure 11B. The results show that the proposed FSS has a stable shielding response for oblique angles of incidence.

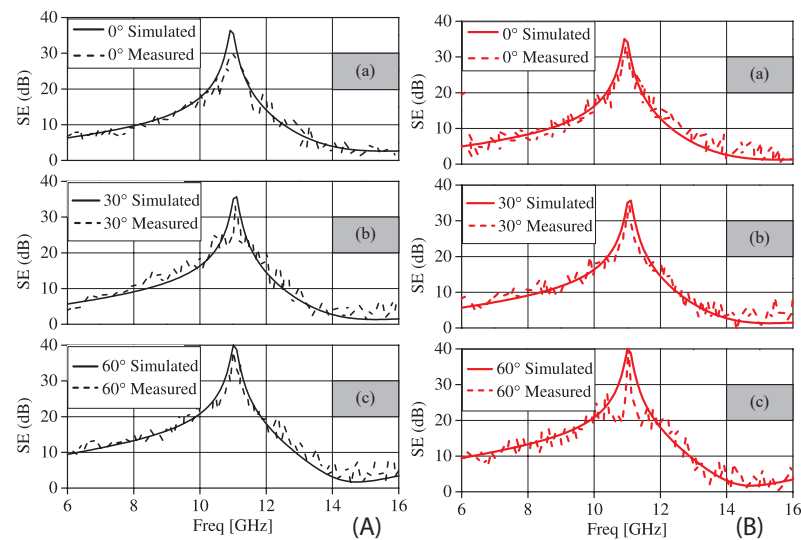


Figure 11. (A) Angular stability analysis of the proposed FSS for the TE/TM polarizations at (a) 0°, (b) 30°, and (c) 60°. (B) Angular stability analysis for the 45° polarization at (a) 0°, (b) 30°, and (c) 60°.

Furthermore, the performance of the proposed FSS with metallic strips (PIN diodes' "ON" state) in suppressing the C-band was also measured for TE/TM and 45° polarization with normal and oblique angles of incidence (0°, 30°, and 60°). The proposed FSS with metallic strips offered 40 dB shielding for the TE/TM polarizations at oblique angles, as is evident in Figure 12A,B. Overall, the stable shielding response and good agreement between the simulation and measured results confirm the employability of the proposed highly compact FSS in applications such as radomes, hospitals, and security areas. It can also be concluded from Figures 11 and 12 that a good agreement between the simulation and measured results exists when the PIN diode equivalent circuit model is used in simulations and metallic strips are used in the measurement to mimic the PIN diodes' "ON" state. The purpose of the PIN diodes in the "ON" state is to provide a continuous current path between the adjacent unit cells of the FSS, whereas the "OFF" state of the PIN diodes disconnects current flow between the unit cells of the FSS. Therefore, the use of the metallic strips for the practical demonstration of the FSS serves the same purpose as that of the "ON" state of the PIN diodes.

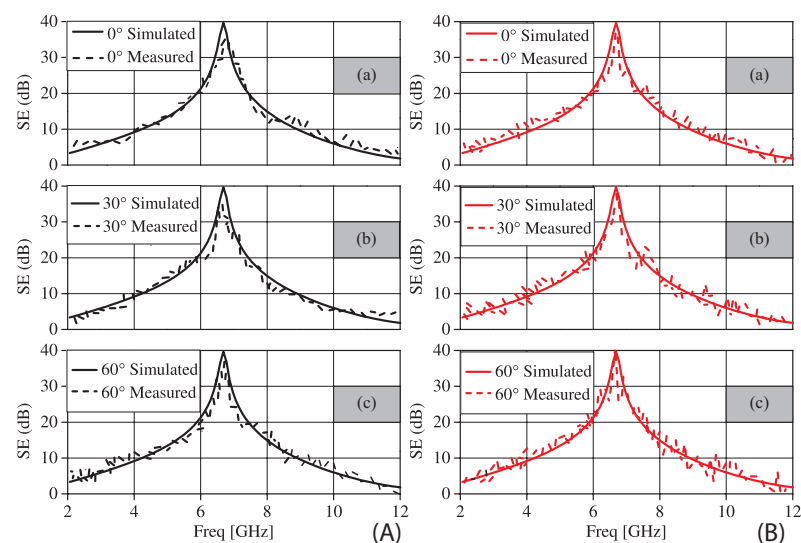


Figure 12. (A) Performance comparison of the FSS with metallic strips for the TE/TM polarization at (a) 0°, (b) 30°, and (c) 60°. (B) Performance comparison for 45° polarization at (a) 0°, (b) 30°, and (c) 60°.

Finally, a comparison table (Table 2) is also included in the manuscript to highlight the novelty of this work in comparison with the other reported reconfigurable/tunable active FSSs. A comparison is sketched between the existing reconfigurable/tunable active FSSs and the proposed active FSS. In addition, a column of reconfigurable techniques is also included in the comparison table to describe the merits and demerits of the previously reported FSSs. In addition to the use of PIN diodes and varactor diodes, mechanical tuning through manual rotation of the FSS has also been reported in literature. However, these manual rotations are not autonomous and require a large mechanical setup for rotation to achieve reconfigurable operation of an FSS. On the other hand, the PIN diodes and associated biasing circuitry are used on the top-side substrate where the shielded structure is designed, which significantly affects the shielding performance of the FSS. In addition, the tunability of an FSS is demonstrated using varactor diodes. Nonetheless, effect of shielding effectiveness still exists because of the coplanar configuration of the FSS, varactor diode, and associated biasing circuitry. The practical demonstration of the proposed FSS validated the employability of the shield in C- and X-band shielding applications, such as in airborne radars and parabolic reflectors for satellite communications.

Table 2. Performance comparison with previously published literature.

Ref.	Reconfigurable/ Tunable Frequencies	Angular Stability/ Polarization	Technique Used	Merits/Demerits
[18]	3.5 GHz, 5 GHz, and 5.8 GHz	Not reported	Mechanical tuning by varying distance	<ul style="list-style-type: none"> • Customized mechanical setup • Not easily applicable for other FSSs • Polarization stability analysis is not possible • A motor is required to rotate the shafts
[19]	12.42 GHz	Up to 30°	PIN diodes	<ul style="list-style-type: none"> • Demonstrated only isolation and no isolation in diodes' ON and OFF states, respectively • Results demonstrated for only 1×3 array
[21]	3.2 GHz, 4.75 GHz, and 5.2 GHz	Up to 60°	Manual rotation of blinds	<ul style="list-style-type: none"> • The rotation of blinds to control EM waves for FSS may not be practical • The FSS structure is difficult to control for frequency reconfigurability
[23]	3.5 GHz–5.7 GHz	Not reported	Varactor Diodes	<ul style="list-style-type: none"> • Additive manufacturing technique is costly • Conformability analysis is provided
[35]	5.7 GHz–9.8 GHz	Up to 30°	PIN Diodes	<ul style="list-style-type: none"> • One parallel bias circuit configuration • Designed on a flexible substrate and offers only 30° angular stability
This work	6.6 GHz and 11 GHz	Up to 60°	PIN Diodes	<ul style="list-style-type: none"> • Biasing circuit on the bottom layer is proposed • Structure is simple and can be printed using cost-effective printing techniques

7. Conclusions

In this paper, a highly compact FSS with unit cell dimensions of $4.8 \text{ mm} \times 4.8 \text{ mm}$ ($0.176\lambda_0 \times 0.176\lambda_0$) was realized in simulations and practically demonstrated using measurements. The optimization of the shielding effectiveness (SE) as a function of the geometric parameters and the substrate's electrical properties was performed in simulations and analytically. It was successfully demonstrated that the proposed FSS provides 25–35 dB SE for the X-band and can be reconfigured to the C-band using PIN diodes installed between the adjacent unit elements. A complete parametric study at normal and oblique angles of

incidence for the TE and TM polarizations is also presented to demonstrate the shielding stability of the proposed FSS with and without metallic strips to mimic the “ON” and “OFF” states of the PIN diodes. Furthermore, an equivalent circuit model (ECM) and mathematical relations for interpreting the dependency of the shielding frequency on the FSS geometry were also formulated using the transmission line theory. The FSS was fabricated and measured to highlight its employability in practical applications. The simulated and measured results agreed well and validated the design concept of the compact FSS for X- and C-band shielding applications.

Author Contributions: U.F. performed the complete simulations. A.I. performed fabrications and measurements. M.F.S. and M.J.M. provided the idea. Post-processing of the results and their comparison were done by M.S.K., A.F., and M.F.S., and D.E.A. assisted in overall paper management, idea development, and manuscript writing. All authors contributed equally to this work. All authors have read and agreed to the published version of the manuscript.

Funding: This work was supported in part by the EU H2020 Marie Skłodowska-Curie Individual Fellowship under Grant # 840854 (VisionRF), and by COMSATS University Islamabad under the COMSATS Research Grant Program (No. 16-65/CGRP/CUI/ISB/18/849).

Conflicts of Interest: The authors declare no conflict of interest.

References

- Chen, N.Z.; Cai, A.; See, T.S.P.; Qing, X.; Chia, M.Y.W. Small planar UWB antennas in proximity of the human head. *IEEE Trans. Microw. Tech.* **2006**, *54*, 1846–1857. [[CrossRef](#)]
- Kara, A.; Bertoni, H.L. Effect of people moving near short-range indoor propagation links at 2.45 GHz. *J. Comm. Net.* **2006**, *8*, 286–289. [[CrossRef](#)]
- Singh, S.; Kapoor, N. Occupational EMF exposure from radar at X and Ku frequency band and plasma catecholamine levels. *Bioelectromagnetic* **2015**, *36*, 444–450. [[CrossRef](#)]
- Hongwei, H. The effect of human activities on 2.4 GHz radio propagation at home environment. In Proceedings of the 2nd IEEE International Conference on Broadband Network Multimedia Technology, Beijing, China, 18–20 October 2009; pp. 95–99.
- Cleary, S.F.; Garber, F.; Liu, L.M. Effects of X-band microwave exposure on rabbit erythrocytes. *Bioelectromagnetics* **1982**, *3*, 453–466. [[CrossRef](#)]
- Munk B A. *Frequency Selective Surfaces-Theory and Design*; John Wiley & Sons: Hoboken, NY, USA, 2000.
- Yadav, S.; Jain, C.P.; Sharma, M.M. Smart phone frequency shielding With penta-bandstop FSS for Security and electromagnetic health applications. *IEEE Trans. Electromagn. Compat.* **2018**, *61*, 887–892. [[CrossRef](#)]
- Farooq, U.; Shafique, M.F.; Mughal, M.J. Polarization insensitive dual band frequency selective surface for RF shielding through glass windows. *IEEE Trans. Electromagn. Compat.* **2020**, *62*, 93–100. [[CrossRef](#)]
- Farooq, U.; Iftikhar, A.; Shafique, M.F.; Mughal, M.J. A miniaturized and polarization insensitive FSS and CFSS for dual band WLAN applications. *Elservier AEU-Int. J. Electron. Comm.* **2019**, *105*, 124–134. [[CrossRef](#)]
- Farooq, U. Ultraminiaturised Polarisation Selective Surface (PSS) for dual-band Wi-Fi and WLAN shielding applications. *IET Microwaves Antennas Propag.* **2020**, *14*, 1514–1521. [[CrossRef](#)]
- Yu, Y.; Chiu, C.; Chiou, Y.; Wu, T. A Novel 2.5-Dimensional ultra-miniaturized-element frequency selective surface. *IEEE Trans. Antennas. Propag.* **2014**, *62*, 3657–3663. [[CrossRef](#)]
- Nauman, M.; Saleem, R.; Rashid, A.K.; Shafique, M.F. A miniaturized flexible frequency selective surface for X-band applications. *IEEE Trans. Electromagn. Compat.* **2016**, *58*, 419–428. [[CrossRef](#)]
- Bagci, F.; Mulazimoglu, C.; Can, S.; Karakaya, E.; Yilmaz, A.E.; Akaoglu, B. A glass based dual band frequency selective surface for protecting systems against WLAN signals. *Int. J. Electron. Commun. (AEU)* **2017**, *82*, 426–434. [[CrossRef](#)]
- Ford, K.L.; Roberts, J.; Zhou, S.; Fong, G.; Rigelsford, J. Reconfigurable frequency selective surface for use in secure electromagnetic buildings. *Electron. Lett.* **2013**, *49*, 861–863. [[CrossRef](#)]
- Majidzadeh, M.; Ghobadi, C.; Nourina, J. A reconfigurable frequency-selective surface for dual-mode multi-band filtering applications. *Int. J. Electron.* **2016**, *104*, 369–381. [[CrossRef](#)]
- Masud, M.M.; Ijaz, B.; Ullah, I.; Braaten, B. A Compact Dual-Band EMI Metasurface shield with an actively tunable polarized lower band. *IEEE Trans. Electromagn. Compat.* **2012**, *54*, 1182–1185. [[CrossRef](#)]
- Bayatpur, F.; Sarabandi, K. Tunable metamaterial frequency-selective surface with variable modes of operation. *IEEE Trans. Microw. Theory Tech.* **2009**, *57*, 1433–1438. [[CrossRef](#)]
- Sivasamy, R.; Moorthy, B.; Kanagasabai, M.; Samsingh, V.R.; Alsath, M.G.N. A wideband frequency tunable FSS for electromagnetic shielding applications. *IEEE Trans. Electromagn. Compat.* **2018**, *60*, 280–283. [[CrossRef](#)]
- Lee, I.-G.; Kim, Y.-J.; Park, Y.-B.; Chun, H.-J.; Hong, I.-P. Design of X-band reconfigurable frequency selective surface with high isolation. *IEICE Electron. Express* **2016**, *13*, 20160567. [[CrossRef](#)]

20. Khaled, E.M.; Atef, E. Design of novel reconfigurable frequency selective surfaces with two control techniques. *Prog. Electromagn. Res.* **2013**, *35*, 135–145.
21. Sundarsingh, S.A.B.E.F.; Ramalingam, V.S. Mechanically Reconfigurable Frequency Selective Surface for RF Shielding in Indoor Wireless Environment. *IEEE Trans. Electromagn. Compat.* **2020**, *62*, 2643–2646.
22. Wang, R.; Cai, L. Liquid Crystal Based Reconfigurable Frequency Selective Surface for ISM Applications. In Proceedings of the 2020 9th Asia-Pacific Conference on Antennas and Propagation (APCAP), Xiamen, China, 4–7 August 2020; pp. 1–2.
23. Tian, T.; Huang, X.; Cheng, K.; Liang, Y.; Hu, S.; Yao, L.; Guan, D.; Xu, Y.; Liu, P. Flexible and Reconfigurable Frequency Selective Surface with Wide Angular Stability Fabricated with Additive Manufacturing Procedure. *IEEE Antennas Wirel. Propag. Lett.* **2020**, *19*, 2428–2432. [[CrossRef](#)]
24. Engineering Simulation & 3D Design Software|ANSYS, HFSS. Available online: www.ansys.com (accessed on 29 June 2018).
25. Getting Started with HFSS: Floquet Ports, Guangzhou Yixi Technology. Available online: <http://www.1cae.com> (accessed on 29 June 2018).
26. Costa, F.; Monorchio, A.; Manara, G. Efficient analysis of frequency-selective surfaces by a simple equivalent-circuit model. *IEEE Antennas Propag. Mag.* **2012**, *54*, 35–48. [[CrossRef](#)]
27. Ghosh, S.; Srivastava, K.V. An equivalent circuit model of FSS-based metamaterial absorber using coupled line theory. *IEEE Antennas Wirel. Propag. Lett.* **2015**, *14*, 511–514. [[CrossRef](#)]
28. Ferreira, D.; Caldeirinha, R.F.S.; Cuiñas, I.; Fernandes, T.R. Square loop and slot frequency selective surfaces study for equivalent circuit model optimization. *IEEE Trans. Antennas Propag.* **2015**, *63*, 3947–3955. [[CrossRef](#)]
29. Joozdani, M.Z.; Amirhosseini, M.K. Equivalent circuit model for the frequency selective surface embedded in a layer With constant Conductivity. *IEEE Trans. Antennas. Propag.* **2017**, *65*, 705–712. [[CrossRef](#)]
30. Yan, M.; Wang, J.; Ma, H.; Qu, S.; Zhang, J.; Xu, C.; Zhang, A. A quad-band frequency selective surface with highly selective characteristics. *IEEE Microw. Wirel. Compon. Lett.*, **2016**, *26*, 562–564. [[CrossRef](#)]
31. Sarabandi, K.; Behdad, N. A frequency selective surface With miniaturized Elements. *IEEE Trans. Antennas. Propag.* **2007**, *55*, 1239–1245. [[CrossRef](#)]
32. Keysight Technologies, Advanced Designed System (ADS). Available online: www.keysight.com (accessed on 20 June 2019).
33. SMP1322-079LF Skyworks Diode-PIN | Skyworks. Available online: <https://store.skyworksinc.com/products/detail/smp1322079lf-skyworks/259214/> (accessed on 20 June 2019).
34. Broadband Horn Antennas. Available online: <http://www.ainfoinc.com> (accessed on 20 June 2019).
35. Lee, I.-G.; Park, Y.-B.; Chun, H.-J.; Kim, Y.-J.; Hong, I.-P. Design of active frequency selective surface with curved composite structures and tunable frequency response. *Hindawi Int. J. Ant. Propag.* **2017**, 1–10. [[CrossRef](#)]